nature physics

SUPPLEMENTARY INFORMATION

https://doi.org/10.1038/s41567-020-0978-6

In the format provided by the authors and unedited.

Universal scaling laws rule explosive growth in human cancers

Víctor M. Pérez-García[1]✉, Gabriel F. Calvo[1], Jesús J. Bosque[1], Odelaisy León-Triana[1], Juan Jiménez[1], Julián Pérez-Beteta[1], Juan Belmonte-Beitia[1], Manuel Valiente[2], Lucía Zhu[2], Pedro García-Gómez[2], Pilar Sánchez-Gómez[3], Esther Hernández-San Miguel[3], Rafael Hortigüela[3], Youness Azimzade[4], David Molina-García[1], Álvaro Martínez[1,5], Ángel Acosta Rojas[6], Ana Ortiz de Mendivil[7], Francois Vallette[8], Philippe Schucht[9], Michael Murek[9], María Pérez-Cano[1], David Albillo[10], Antonio F. Honguero Martínez[11], Germán A. Jiménez Londoño[12], Estanislao Arana[13] and Ana M. García Vicente[12]

[1]Mathematical Oncology Laboratory, Universidad de Castilla–La Mancha, Ciudad Real, Spain. [2]Brain Metastasis Group, Spanish National Cancer Research Centre (CNIO), Madrid, Spain. [3]Neuro-oncology Unit, Health Institute Carlos III-UFIEC, Madrid, Spain. [4]Department of Physics, University of Tehran, Tehran, Iran. [5]Department of Mathematics, Universidad de Cádiz, Cádiz, Spain. [6]Department of Radiation Oncology, Sanchinarro University Hospital, HM Hospitales, Madrid, Spain. [7]Department of Neuroradiology, Sanchinarro University Hospital, HM Hospitales, Madrid, Spain. [8]Inserm U1232, Centre de Recherche en Cancérologie et Immunologie Nantes-Angers, Nantes, France. [9]Neurosurgery Clinic, Bern Insespital, Bern, Switzerland. [10]Radiology Unit, MD Anderson Cancer Center, Madrid, Spain. [11]Thoracic Surgery Unit, Hospital General Universitario de Albacete, Albacete, Spain. [12]Nuclear Medicine Unit, Hospital General Universitario de Ciudad Real, Ciudad Real, Spain. [13]Fundación Instituto Valenciano de Oncología, Valencia, Spain.
✉e-mail: victor.perezgarcia@uclm.es

Supplementary information for "Universal scaling laws rule explosive growth in human cancers"

Víctor M. Pérez-García[1]*, Gabriel F. Calvo[1], Jesús J. Bosque[1], Odelaisy León-Triana[1], Juan Jiménez[1], Julián Pérez-Beteta[1], Juan Belmonte-Beitia[1], Manuel Valiente[2], Lucía Zhu[2], Pedro García-Gómez[2], Pilar Sánchez-Gómez[3], Esther Hernández-San Miguel[3], Rafael Hortigüela[3], Youness Azimzade[4], David Molina-García[1], Álvaro Martínez[1,5], Ángel Acosta-Rojas[6], Ana Ortiz de Mendivil[7], Francois Vallette[8], Philippe Schucht[9], Michael Murek[9], María Pérez-Cano[1], David Albillo[10], Antonio F. Honguero Martínez[11], Germán A. Jiménez Londoño[12], Estanislao Arana[13] & Ana M. García Vicente[12]

[1]Mathematical Oncology Laboratory, Universidad de Castilla-La Mancha, Spain; [2]Brain Metastasis Group, Spanish National Cancer Research Centre (CNIO), Madrid, Spain; [3]Neuro-oncology Unit, Health Institute Carlos III-UFIEC, Madrid, Spain; [4]Department of Physics, University of Tehran, Iran; [5]Department of Mathematics, Universidad de Cádiz, Spain; [6]Department of Radiation Oncology, Sanchinarro University Hospital, HM Hospitales, Spain; [7]Department of Neuroradiology, Sanchinarro University Hospital, HM Hospitales, Spain; [8] Inserm U1232, Centre de Recherche en Cancérologie et Immunologie Nantes-Angers, Nantes, F-44007, France; [9]Neurosurgery Clinic, Bern Insespital, Switzerland; [10]Radiology Unit, MD Anderson Cancer Center, Madrid, Spain; [11]Thoracic Surgery Unit, Hospital General Universitario de Albacete, Spain; [12]Nuclear Medicine Unit, Hospital General Universitario de Ciudad Real, Spain; [13]Fundación Instituto Valenciano de Oncología, Spain.

*Corresponding author: victor.perezgarcia@uclm.es

8 June 2020

S1. Allometric scaling equation

We begin by considering the metabolic rate of a tumour to be $B \propto V^{\beta}$, where V is the total volume occupied by viable cells and $\beta > 0$ is the scaling exponent. Due to energy conservation, the temporal dynamics of tumour growth is given by $B = aV + b\frac{dV}{dt}$, where the first and second right-hand terms represent cell maintenance and proliferation, respectively [1]. The resulting first-order differential equation describing the time variation of $V = V(t)$ can thus be written as

$$\frac{dV}{dt} = -\gamma V + \alpha V^{\beta}, \tag{S1}$$

with $\gamma > 0$ and an initial condition for the tumour volume at time $t = t_0$, $V(t_0) = V_0$. This is a Bernoulli-type ordinary differential equation (ODE) when $\beta \neq 1$. The substitution $z(t) = V^{1-\beta}$ transforms (S1) into a linear ODE

$$\frac{dz}{dt} = (1-\beta)(\alpha - \gamma z), \tag{S2}$$

which can be solved exactly. The solution in closed form for $V(t)$ is

$$V(t) = \left[\frac{\alpha - \left(\alpha - \gamma V_0^{1-\beta}\right) e^{\gamma(\beta-1)(t-t_0)}}{\gamma}\right]^{1/(1-\beta)}. \tag{S3}$$

If $\beta > 1$, Eq. (S3) blows up in a finite time t_{crit} given by

$$t_{\text{crit}} = t_0 + \frac{1}{(\beta-1)\gamma} \log\left(\frac{\alpha}{\alpha - \gamma V_0^{1-\beta}}\right). \tag{S4}$$

The case $\alpha - \gamma V_0^{1-\beta} < 0$ corresponds to initial data with tumours having nutrient demands exceeding the supplies, thus we focus on the case $\alpha - \gamma V_0^{1-\beta} > 0$.

For highly aggressive tumours the contribution of the term $-\gamma V$, associated with cell death, is much smaller than that of proliferation. Hence, neglecting such a linear term, which is equivalent to letting $\gamma \to 0$, reduces (S3) and (S4), respectively, to the formulas used in the main text of the work

$$V(t) = \left[V_0^{1-\beta} - \alpha(\beta-1)(t-t_0)\right]^{1/(1-\beta)}, \tag{S5}$$

$$t_{\text{crit}} = t_0 + \frac{V_0^{1-\beta}}{(\beta-1)\alpha}. \tag{S6}$$

S2. Derivation and analysis of the continuous volume-dependent proliferation-rate model

S2.1. Introduction

Here we shall both provide a derivation and study in some detail the dynamics of the continuous spatio-temporal model

$$\frac{\partial u}{\partial t} = D\nabla^2 u + (\rho_0 + \rho_1 N(t))\left(1 - \frac{u}{K}\right)u, \tag{S7}$$

where $u = u(\mathbf{x}, t)$ is the tumour cell density, which is a function of space $\mathbf{x}$ and time t. The parabolic equation (S7) represents a non-local extension of the well-known Fisher-Kolmogorov partial differential equation [2]. The first term on the right-hand side of (S7) accounts for tumour cell migration that results in invasion of the surrounding tissue, with $D > 0$ denoting a characteristic cell diffusion constant. The second term on the right-hand side of (S7) reflects tumour cell proliferation. Here, $\rho_0 > 0$ and $\rho_1 \geq 0$ are the size-independent and size-dependent effective proliferation rates, respectively. When $\rho_1 = 0$, the standard (local) Fisher-Kolmogorov equation is recovered. If, however, $\rho_1 > 0$, Equation (S7) becomes non-local because it depends on the total number of cells

$$N(t) = \int_{\Omega} u(\mathbf{x}, t)\, d^3\mathbf{x}, \tag{S8}$$

with Ω denoting a sufficiently large volume containing the full tumour over its entire development, or the whole $\mathbb{R}^d$, where d

is the spatial dimension ($d = 1, 2$, or 3). This model adds spatial information with respect to the previous model (S1) and regards that the total proliferation rate may depend on tumour size, on the grounds that a larger tumour will lead to higher accumulated mutational events.

Equation (S7) is supplemented with homogeneous Neumann boundary conditions (no cell flux) $\partial u/\partial \mathbf{n} = 0$, $\forall \mathbf{x} \in \partial\Omega$, where $\mathbf{n}$ is the vector normal to the boundary $\partial\Omega$, together with an initial condition $u(\mathbf{x}, t = t_0) = u_0(\mathbf{x})$, which represents the tumour cell-density distribution at some instant $t = t_0$. In our simulations, $u_0(\mathbf{x})$ was initially assumed to be very small and highly localized (e.g. a carcinoma *in situ*), so as to describe an emergent tumour that unfolds in time.

One key dynamical quantity to be analysed later on is the total proliferation activity (or metabolic rate) which, in the context of the above model (S7), can be defined as

$$M(t) = \frac{dN}{dt} = (\rho_0 + \rho_1 N(t)) \int_\Omega \left(1 - \frac{u}{K}\right) u \, d^3\mathbf{x}. \qquad \text{(S9)}$$

The right-hand side of this expression readily follows from integrating (S7) over the domain Ω and imposing the Neumann boundary conditions.

It will also be convenient to introduce unitless time $\tau = \rho_0 t$ and space $\boldsymbol{\xi} = \sqrt{\rho_0/D}\,\mathbf{x}$ variables, together with a normalised cell density $u(\boldsymbol{\xi}, \tau) \equiv u/K$. Hence, (S9) reads as

$$M(\tau) = (1 + \eta N(\tau)) \int_\Omega (1 - u)\, u \, d^3\boldsymbol{\xi}, \qquad \text{(S10)}$$

where $\eta = \rho_1 K D^{d/2}/\rho_0^{(d+2)/2}$. Thus, the non-local Fisher-Kolmogorov equation (S7) can be cast as a one-parameter model, which makes its formal analysis simpler.

For sufficiently long times, the angular dependencies of the solutions of the FK equation become negligible with respect to the distance variable. To identify the underlying scalings of (S7), it suffices to focus on the radial dependence in u. Thus, in (S10), the differential element reduces to $d^3\boldsymbol{\xi} = B^{(d)}\xi^{d-1}d\xi$, where $B^{(1)} = 2$, $B^{(2)} = 2\pi$ and $B^{(3)} = 4\pi$, with $\xi \in [0, \infty)$ being the radial variable.

S2.2. Derivation of the non-local Fisher-Kolmogorov model

We begin by considering the tumour cell population to be structured both by its spatial position vector $\mathbf{x} \in \Omega \subset \mathbb{R}^d$ and by a net proliferation rate $\rho \in [0, \rho_{\max}]$, where $\rho_{\max}$ represents a maximum proliferation rate (for practical purposes it can be taken sufficiently large since it does not restrict our analysis). Let $w = w(\mathbf{x}, \rho, t)$ denote a cell density function such that $w(\mathbf{x}, \rho, t)d^3\mathbf{x}d\rho$ is the number of tumour cells that, at time t, have a proliferation rate ρ at point $\mathbf{x}$. We describe the dynamics of $w(\mathbf{x}, \rho, t)$ via the following migration-selection-mutation integro-differential equation:

$$\begin{aligned}\frac{\partial w}{\partial t} &= D_{\rm m}(\rho)\nabla^2 w + D_\rho \frac{\partial^2 w}{\partial \rho^2} \\ &+ \left(\rho + \nu \int_\Omega \int_0^{\rho_{\max}} \rho' \mathcal{M}(\rho, \rho') w(\mathbf{x}', \rho', t) d^3\mathbf{x}' d\rho'\right) \\ &\times \left(1 - \frac{1}{K}\int_0^{\rho_{\max}} w(\mathbf{x}, \rho', t) d\rho'\right) w(\mathbf{x}, \rho, t)\,. \qquad \text{(S11)}\end{aligned}$$

The first term on the right-hand-side accounts for cell migration with a diffusion constant $D_{\rm m}(\rho)$ that generally depends on the proliferation rate of that cell subpopulation. The second term captures the effect of non-genetic instability, which is mediated by fluctuations in the proliferation phenotype that take place with a diffusion rate D_ρ. The proliferation phenotype is a hallmark in tumours resulting from alterations in growth regulation [3]. The third term consists of two main factors. The first factor comprises selection plus the effect of genetic mutations. Those cells with a larger ρ will tend to have a fitness advantage unless exogenous mechanisms exert a detrimental action on such cells. The kernel $\mathcal{M}(\rho, \rho')$ represents the probability that the mutation of a cell with proliferation rate ρ' gives rise to a daughter cell having a proliferation rate ρ. For a genetic change to occur it is necessary a proliferative event, which explains the presence of ρ' in the integral. Notice also that an integration over all cells experiencing a mutation resulting in a proliferation rate ρ is taken weighted by the positive constant ν. Such an integration reflects the collective impact of the tumour microenvironment in promoting genetic mutations. The second factor corresponds to cell saturation with a carrying capacity K (maximum number of cells per unit volume), avoiding arbitrarily large densities.

Upon integration of (S11) over ρ and making use of the mean value theorem for integrals, together with $\int_0^{\rho_{\max}} w(\mathbf{x}, \rho, t)d\rho = u(\mathbf{x}, t)$, we get the following expressions

$$\int_0^{\rho_{\max}} \left(\frac{\partial w}{\partial t}\right) d\rho = \frac{\partial u}{\partial t}, \qquad \text{(S12)}$$

$$\int_0^{\rho_{\max}} \left(D_{\rm m}(\rho)\nabla^2 w\right) d\rho = D\nabla^2 u, \qquad \text{(S13)}$$

$$\int_0^{\rho_{\max}} \left(D_\rho \frac{\partial^2 w}{\partial \rho^2}\right) d\rho = D_\rho \frac{\partial w}{\partial \rho}\bigg|_0^{\rho_{\max}}, \qquad \text{(S14)}$$

$$\int_0^{\rho_{\max}} \rho w(\mathbf{x}, \rho, t) d\rho = \rho_0\, u(\mathbf{x}, t), \qquad \text{(S15)}$$

where D and ρ_0 denote positive characteristic cell diffusion constant and size-independent proliferation rate, respectively. If we further impose zero-flux boundary conditions on (S14), then this contribution vanishes. Also,

$$\begin{aligned}&\int_0^{\rho_{\max}} \left(\int_\Omega \int_0^{\rho_{\max}} \rho' \mathcal{M}(\rho, \rho') w(\mathbf{x}', \rho', t) d^3\mathbf{x}' d\rho'\right) w(\mathbf{x}, \rho, t) d\rho \\ &= \int_\Omega \int_0^{\rho_{\max}} \rho' w(\mathbf{x}', \rho', t) d^3\mathbf{x}' d\rho' \\ &\times \left(\int_0^{\rho_{\max}} \mathcal{M}(\rho, \rho') w(\mathbf{x}, \rho, t) d\rho\right) \\ &= u(\mathbf{x}, t) \int_\Omega \int_0^{\rho_{\max}} \rho' \mathcal{M}(\rho^*, \rho') w(\mathbf{x}', \rho', t) d^3\mathbf{x}' d\rho' \\ &= \rho_1\, u(\mathbf{x}, t) \int_\Omega u(\mathbf{x}', t) d^3\mathbf{x}' = \rho_1\, u(\mathbf{x}, t) N(t), \qquad \text{(S16)}\end{aligned}$$

where $\rho_1 \geq 0$ is a characteristic size-dependent proliferation rate. By combining the above expressions in (S11) we finally arrive at the non-local Fisher-Kolmogorov equation (S7). Notice that in the absence of mutations, which would correspond to $\mathcal{M}(\rho, \rho') = 0$, we recover the standard (local) FK equation.

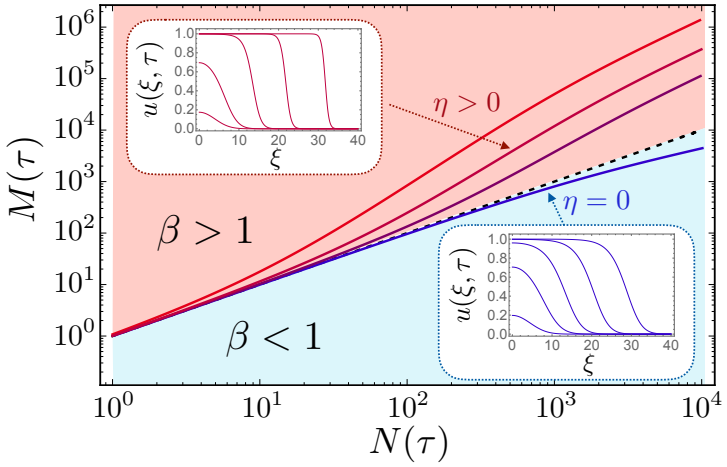

Figure S1 Local and non-local Fisher-Kolmogorov models lead to different allometric scaling laws. The main plot represents the dependence of the metabolic rate $M(\tau)$ versus the total tumour cell number $N(\tau)$. The lines represent trajectories $(M(\tau), N(\tau))$ obtained from numerical simulations of Eq. (S7) and different values of the dimensionless parameter η. The shadings indicate the exponents in each region, light blue $\beta < 1$, coral $\beta > 1$. Simulations with $\eta = 0$, corresponding to the local Fisher-Kolmogorov equation, provide a sublinear exponent $\beta = 2/3$ (blue line). Travelling wave solutions develop from the initial data with a fixed profile and interface width during propagation (bottom right inset). Simulations with different values of $\eta > 0$ (non-local FK equation) show superlinear behaviour with β close to 4/3, for sufficiently long times τ. The upper left inset shows the sharpening profiles indicating the acceleration of the front. The black dashed line marks the $\beta = 1$ threshold separating sublinearity from superlinearity.

S2.3. Allometric scaling laws in the non-local Fisher-Kolmogorov model are bounded from above by a superlinear scaling law with $\beta \leq 2$

The solution $u(\boldsymbol{\xi},\tau)$ of the non-local Fisher-Kolmogorov equation satisfies $0 \leq u \leq 1$ everywhere. This implies that $(1-u)\,u \leq u$. It then follows from (S10) that the metabolic rate is equal to

$$\begin{aligned} M(\tau) &= (1+\eta N(\tau)) \int_\Omega (1-u)\,u\, d^3\boldsymbol{\xi} \\ &\leq (1+\eta N(\tau)) \int_\Omega u\, d^3\boldsymbol{\xi} \\ &= N(\tau) + \eta N^2(\tau). \end{aligned} \tag{S17}$$

As a consequence, the non-local Fisher-Kolmogorov model is bounded from above by an allometric scaling with exponent $\beta \leq 2$ if $\eta > 0$. Thus, (S17) provides a supersolution for (S9) given by

$$N_{\text{sup}}(\tau) = \frac{N_0 e^{\tau-\tau_0}}{1+\eta N_0 - \eta N_0 e^{\tau-\tau_0}}, \tag{S18}$$

where N_0 is the number of tumour cells at $\tau = \tau_0$. From (S18), an upper bound for the blow-up time is given by

$$\tau_{\text{crit}} = \tau_0 + \log\left(\frac{1+\eta N_0}{\eta N_0}\right). \tag{S19}$$

This time decreases as η increases.

S2.4. Allometric scaling laws in the local Fisher-Kolmogorov model are sublinear

We wish to find under what conditions there is a scaling relation between $M(\tau)$ and $N(\tau)$ (or equivalently the tumour volume) displaying a superlinear exponent (i.e. $\beta > 1$). It is instructive to first briefly examine the local Fisher-Kolmogorov equation. If $\eta = 0$ (which occurs when $\rho_1 = 0$), then (S10) reduces to

$$M_{\text{FK}}(\tau) = B^{(d)} \int_0^\infty \xi^{d-1}\,(1-u)\,u\, d\xi \equiv B^{(d)} I_{\text{FK}}^{(d)}(\tau). \tag{S20}$$

For sufficiently long times τ, the solution to the d-dimensional local Fisher-Kolmogorov equation satisfies $u \simeq 1$ up to the wave front, which propagates with a stable and invariant profile whose position (at half height) is $\xi_{\text{FK}}(\tau)$, while its width is a constant $2\sigma_{\text{FK}}$ (that may generally depend on d). For $\xi \gg \xi_{\text{FK}}(\tau)$, $u \simeq 0$. The bottom right inset in Figure S1 depicts the numerical solution of the local Fisher-Kolmogorov equation in 3D. The wave front tends to move with a constant velocity equal to 2 (or $2\sqrt{D\rho_0}$ in the original units).

The integral $I_{\text{FK}}^{(d)}(\tau)$ in (S20) can be accurately approximated by

$$\begin{aligned} I_{\text{FK}}^{(d)}(\tau) &\simeq \frac{1}{4d}\left[(\xi_{\text{FK}}(\tau)+\sigma_{\text{FK}})^d - (\xi_{\text{FK}}(\tau)-\sigma_{\text{FK}})^d\right] \\ &\simeq \frac{\xi_{\text{FK}}^{d-1}(\tau)\sigma_{\text{FK}}}{2}, \end{aligned} \tag{S21}$$

provided that $\xi_{\text{FK}}(\tau) \gg \sigma_{\text{FK}}$, which is satisfied asymptotically. Moreover, over the long time-scale, total cell number can be approximated by

$$N_{\text{FK}}(\tau) \simeq B^{(d)} \int_0^\infty \xi^{d-1} u(\xi,\tau)\, d\xi \simeq \frac{B^{(d)} \xi_{\text{FK}}^d(\tau)}{d}. \tag{S22}$$

Combining (S21) and (S22) into (S20) we get the following relation between metabolic rate and total cell number when the dynamics is governed by a d-dimensional local Fisher-Kolmogorov equation

$$M_{\text{FK}}(\tau) \simeq \frac{B^{(d)}\sigma_{\text{FK}}}{2}\left(\frac{N_{\text{FK}}(\tau) d}{B^{(d)}}\right)^{(d-1)/d}. \tag{S23}$$

This last expression shows that, within a d-dimensional local Fisher-Kolmogorov model, the allometric scaling law is sublinear, because the exponent $\beta = \frac{d-1}{d} < 1$. Hence, there cannot be explosive tumour growth in this scenario.

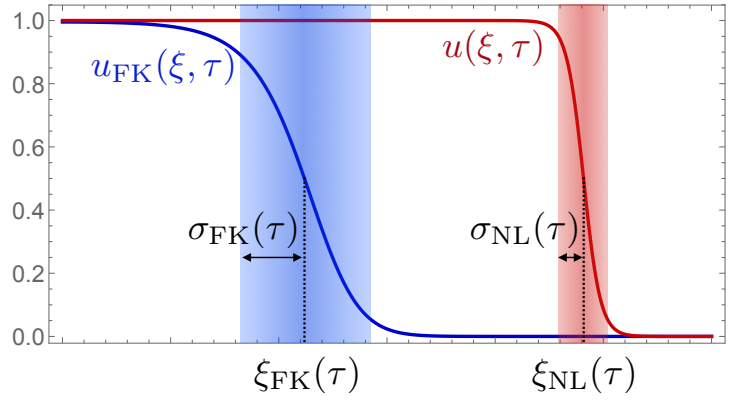

Figure S2 The solution to the non-local Fisher-Kolmogorov model accelerates with respect to the local solution and its width decreases. Comparison of the full solution $u(\xi,\tau)$ to the non-local Fisher-Kolmogorov and the local solution $u_{\rm FK}(\xi,\tau)$. The wave front positions (at half height) and half widths are $\xi_{\rm NL}(\tau)$, $\xi_{\rm FK}(\tau)$, $\sigma_{\rm NL}(\tau)$ and $\sigma_{\rm FK}(\tau)$, respectively.

S2.5. The Allometric scaling law in the 3D nonlocal Fisher-Kolmogorov model is superlinear

Let us now turn to the full non-local Fisher-Kolmogorov model where $\eta > 0$ (i.e. $\rho_1 > 0$). To gain insight, we refer to the upper left inset in Figure S1. Our numerically calculated profiles for $u(\xi,\tau)$ show that, as the wave front progresses, the velocity increases and the steepness grows without bound, tending towards a shock wave.

We will follow the same rationale as in the previous subsection. For sufficiently long times τ, the full solution to the d-dimensional non-local Fisher-Kolmogorov equation satisfies $u \simeq 1$ up to the wave front, whose position (at half height) is $\xi_{\rm NL}(\tau)$ and accelerates, while its width $2\sigma_{\rm NL}(\tau)$ decreases towards zero. This means that, when comparing the wave front propagation of the solution $u_{\rm FK}$ of the local Fisher-Kolmogorov equation to the full non-local solution, it will lag behind the wave front of u for the same initial data. Figure S2 illustrates the behaviour of both solutions schematically.

Using (S10) and working again in radial variables, we have

$$\begin{aligned} M(\tau) &= (1+\eta N(\tau))B^{(d)}\int_0^\infty \xi^{d-1}\,(1-u)\,u\,d\xi \\ &\equiv (1+\eta N(\tau))B^{(d)} I^{(d)}_{\rm NL}(\tau). \end{aligned} \tag{S24}$$

The integral $I^{(d)}_{\rm NL}(\tau)$ can be approximated as $I^{(d)}_{\rm FK}(\tau)$ and its expression is given by

$$\begin{aligned} I^{(d)}_{\rm NL}(\tau) &\simeq \frac{1}{4d}\left[(\xi_{\rm NL}(\tau)+\sigma_{\rm NL}(\tau))^d - (\xi_{\rm NL}(\tau)-\sigma_{\rm NL}(\tau))^d\right] \\ &\simeq \frac{\xi^{d-1}_{\rm NL}(\tau)\sigma_{\rm NL}(\tau)}{2}, \end{aligned} \tag{S25}$$

where we have used the fact that $\sigma_{\rm NL}(\tau) \ll \xi_{\rm NL}(\tau)$.

The behaviour of the product $\xi_{\rm NL}(\tau)\sigma_{\rm NL}(\tau)$ has been studied numerically. This was done by solving Eq. (S7) numerically using a combination of finite difference schemes and Newton-Cotes quadratures. As initial data we considered small density-amplitude and localized tumours with a given Gaussian distribution $u_0(\mathbf{x})$. Our simulations revealed that $\xi_{\rm NL}(\tau)\sigma_{\rm NL}(\tau)$ tends towards a non-zero constant μ that increases with η. Therefore,

$$I^{(d)}_{\rm NL}(\tau) \simeq \frac{\mu\,\xi^{d-2}_{\rm NL}(\tau)}{2}. \tag{S26}$$

Moreover, in the long time regime, the total number of cells can be approximated by

$$N(\tau) \simeq B^{(d)}\int_0^\infty \xi^{d-1}u(\xi,\tau)\,d\xi \simeq \frac{B^{(d)}\xi^d_{\rm NL}(\tau)}{d}. \tag{S27}$$

Combining Eqs. (S26) and (S27) into (S24) we get the following relation between metabolic rate and total cell number when the dynamics is governed by the d-dimensional non-local Fisher-Kolmogorov equation

$$M(\tau) \simeq \frac{B^{(d)}\mu}{2}\,(1+\eta N(\tau))\left(\frac{N(\tau)d}{B^{(d)}}\right)^{(d-2)/d}. \tag{S28}$$

In contrast with Eq. (S23), Eq. (S28) shows that, when $d = 3$, the non-local Fisher-Kolmogorov model leads to a superlinear allometric scaling law because the dominating exponent is $\beta = \frac{4}{3} > 1$. However, for $d \leq 2$, the exponent cannot be superlinear and no blow-up occurs.

To gain additional insight of why the scaling exponent β cannot be superlinear in lower spatial dimensions, one has to take into account that when cells proliferate they need a certain amount of available space (embodied by the carrying capacity K within the NLFK model). If $d < 3$, cells reduce their *effective clustering occupancy*. That is, they would need to migrate to more distant regions thus decreasing the interaction with other competing subpopulations or else inhibit their proliferation since they saturate earlier the available space. This eventually precludes an exploding total proliferation activity $M(t)$, albeit $M(t)$ can still grow at an exponential rate for $d = 2$.

To conclude this section, we should mention that Eq. (S7) admits the following extension

$$\frac{\partial u}{\partial t} = D\nabla^2 u + \Big(\rho_0 + \rho_1 N^\lambda(t)\Big)\Big(1-\frac{u}{K}\Big)\,u, \tag{S29}$$

where $\lambda \geq 0$ is an exponent associated to the size-dependent growth. The exponent λ characterises whether the entire tumour volume contributes to an increase in proliferation, which occurs when $\lambda = 1$, or else it is related to a fractal dimension of the tumour. For instance, if $\lambda = 2/3$, only a thin layer of cells at the tumour surface would contribute to the acceleration of growth. By adapting the previous analysis, the dominating exponent $\beta = 1+\lambda-\frac{2}{d}$, meaning that only if $\lambda > 2/3$ we would expect blow-up. Moreover, the λ exponent would also reflect effects related to the irregularity of the tumour [4].

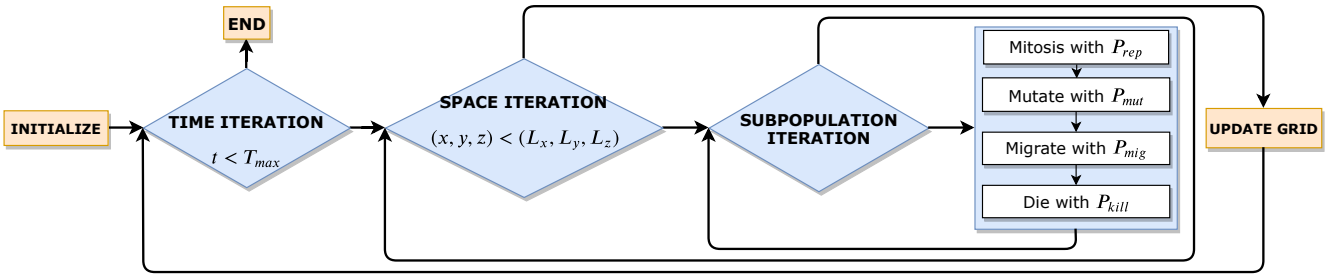

Figure S3 Model workflow scheme. Basic model outline (for implementation purposes). Initialization requires to set spatial domain and time span, to define clonal population properties, and to place initial cells in a given voxel (or several of them). After that first step, time iterations are carried out until a maximum time is reached. At each time step, every voxel is evaluated; and at each voxel, all clonal populations are updated. This updating require first the calculation how many cells are going to reproduce, migrate, mutate or die per voxel; and then all of them are updated simultaneously.

S3. Stochastic mesoscale tumour growth simulator

In order to further elucidate how different interacting cell populations influence tumour evolutionary dynamics, we developed a stochastic mesoscale tumour growth simulator. Typical cellular automata or other individual-based approaches based on cells cannot simulate tumours in volume ranges of $10{-}100$ cm^3, that contain up to 10^{12} cells. Individual-based approaches would demand huge computational resources to simulate those amounts of cells in clinically relevant time scales (from months to several years). Thus, we opted for a different mesoscale simulation approach. By mesoscale we refer to a level of spatial detail where clinically relevant tumour sizes are reachable at the cost of cellular resolution, which is partially lost.

The model describes the spatio-temporal dynamics of several competing tumour cell subpopulations and incorporates four basic cellular processes: replication, death, migration and mutation. Cells undergo these processes at different rates, depending on the genetic/phenotypic characteristics of the clonal population they belong to. Cells in the same clonal population have the same properties, except for the microenvironmental conditions and an intrinsic noise coming from stochastic transitions. The spatial domain where these clonal populations will compete is a 3D mesh of L^3 elements (voxels). Each voxel is a compartment where many cells may coexist in each subpopulation. The size of these compartments (Δx) has been selected to resemble the voxels sizes typically available in high-resolution medical imaging (around 1 mm^3).

Instead of iterating along each cell in each voxel at every time step, whole clonal populations are evaluated at once. At each iteration, it must be determined how clonal populations change their number. This is carried out by calculating the amount of cells that duplicate, die, move to a neighbouring voxel, or mutate. By randomly sampling from binomial distributions with probabilities calculated accordingly it is possible to assess the clonal populations. To further illustrate this, we can consider a single cell attempting to divide. It will have two possible outcomes: success or failure, with excluding probabilities. This is none but a Bernoulli experiment. So, if we can draw a cell's dividing outcome by randomly sampling from a Bernoulli distribution, the outcome of a whole clonal population with N_{subpop} cells can be drawn by randomly sampling from a Binomial distribution with N_{subpop} experiments. The probabilities for each process and clonal populations are calculated at each time step inside each voxel by the equations

$$P_{\text{rep}} = \frac{\Delta t}{\tau_{\text{rep}}}\left(1 - \frac{N+D}{K}\right), \tag{S30a}$$

$$P_{\text{mig}} = \frac{\Delta t}{\tau_{\text{mig}}\Delta x^2}\left(\frac{N+D}{K}\right), \tag{S30b}$$

$$P_{\text{kill}} = \frac{\Delta t}{\tau_{\text{kill}}}\left(\frac{N+D}{K}\right), \tag{S30c}$$

$$P_{\text{mut}} = \frac{\Delta t}{\tau_{\text{mut}}}\left(\frac{N_{\text{subpop}}}{K}\right), \tag{S30d}$$

where $1/\tau$ are the rates associated to a given cellular process; N and D are respectively the number of alive and dead cells in a voxel, and K is the voxel carrying capacity. The less crowded a voxel is, the more likely it will be for cells to divide, while chances of migration and death will be reduced. This leads to logistic-like growth curves for each voxel in the absence of death and interactions with other voxels. Mutation only depends on the number of cells from a given clonal population.

Mathematically, the evolution of the clonal populations is computed using the equation

$$N^{i,j,k}_{n,t+1} = N^{i,j,k}_{n,t} + N^{i,j,k}_{n_{\text{rep}},t} - N^{i,j,k}_{n_{\text{kill}},t} - N^{i,j,k}_{n_{\text{mut}},t} + N^{i,j,k}_{n'_{\text{mut}},t} - N^{i,j,k}_{n_{\text{mig}},t} + N^{i',j',k'}_{n_{\text{mig}},t}, \tag{S31}$$

where t is the discrete time index, n is the clonal population index, $\{i,j,k\}$ are the voxel's discrete spatial coordinates, and $\{i',j',k'\}$ represent spatial coordinates of neighbouring voxels. $N^{i,j,k}_{n,t}$ is number of cells in each clonal population n at voxel i,j,k and time t. Thus, a clonal population updates its cell number by adding to its previous state (1st right-hand term) newborn cells (2nd right-hand term), cells coming from other clonal populations that mutate into the evaluated one (5th right-hand term), and cells coming from surrounding voxels (7th right-hand term); and by subtracting dead cells (3rd right-hand term), cells mutating into a different clonal subpopulation (4th right-hand term), and cells migrating from the current voxel to surrounding ones (6th right-hand term).

Contributions are randomly sampled at each time step from binomial distributions using the probabilities (S30) and the

Model parameters			
Parameters	Description	Units	Values
L	Number of voxels per side	-	80
Δx	Voxel side length	[mm]	1
Δt	Time step length	[hours]	24
K	Carrying capacity per voxel	[cells]	$2 \cdot 10^5$
N_0	Initial population	[cells]	1
$N_{\text{threshold}}$	Minimum cell number to consider a voxel occupied	[cells]	$0.2 \cdot K$
V_{end}	Maximum tumour volume	[cm^3]	100
$1/\tau_{\text{rep}}$	Proliferation rates	[h^{-1}]	$[1.3 \cdot 10^{-3} - 5 \cdot 10^{-4}]$
$1/\tau_{\text{mig}}$	Migration rates	[h^{-1}]	$[1.7 \cdot 10^{-3} - 4 \cdot 10^{-4}]$
$1/\tau_{\text{kill}}$	Death rate	[h^{-1}]	$[1 \cdot 10^{-3} - 3.3 \cdot 10^{-4}]$
$1/\tau_{\text{mut}}$	Mutation rates	[h^{-1}]	$[1 \cdot 10^{-3} - 1 \cdot 10^{-6}]$

Table S1 Parameters of the model used for the stochastic mesoscale tumour growth simulator

Population's weights				
Process	Clonal pop. 1	Clonal pop. 2	Clonal pop. 3	Clonal pop. 4
Duplication	1	1.2	1.44	1.8
Migration	1	1.1	1.2	1.3
Death	1	0.85	0.65	0.5
Mutation	1	2	4	-

Table S2 Weights associated to each population in the simulations

equations

$$N^{i,j,k}_{n_{\text{rep}},t} \sim B\left(N^{i,j,k}_{\sum n,t}, P_{\text{rep}}\right), \tag{S32a}$$

$$N^{i,j,k}_{n_{\text{kill}},t} \sim B\left(N^{i,j,k}_{\sum n,t}, P_{\text{kill}}\right), \tag{S32b}$$

$$N^{i,j,k}_{n_{\text{mig}},t} \sim B\left(N^{i,j,k}_{\sum n,t}, P_{\text{mig}}\right), \tag{S32c}$$

$$N^{i,j,k}_{n_{\text{mut}},t} \sim B\left(N^{i,j,k}_{n,t}, P_{\text{mut}}\right). \tag{S32d}$$

A mutation (or phenotypic change) process requires defining a tree, along which cellular subpopulations can evolve as a Markov chain. Depending on whether this tree is linear, i.e. cells jump from a given clonal population to another in a stepwise way via mutation events, or branched in which cells may jump to different clonal populations from a given one, clonal populations become more aggressive as they increase the number of mutations they carry. This aggressiveness is translated into faster mitosis and migration ratios in the model; changes in these rates will be modulated by weights associated to each mutation. Migration is more intricate, as migrating cells will tend to be distributed in the surrounding voxels. Once we compute how many cells leave a voxel via (S32), their distribution (von Neumann neighbourhood, 6 surrounding voxels in 3D) is determined by randomly sampling from a multinomial distribution, whose probabilities depend on the cell gradient between voxels, mathematically

$$\begin{cases} \mathbf{N}^r_{n_{\text{mig}},t} \sim M(N^{i,j,k}_{n_{\text{mig}},t}, \mathbf{P}_{\text{dist},r}), \\ \mathbf{P}_{\text{dist},r} = \alpha \dfrac{N^{i,j,k}_{n,t} - N^r_{n,t}}{\sum\limits_{r=1}^{6}\left(N^{i,j,k}_{n,t} - N^r_{n,t}\right)}, \end{cases} \tag{S33}$$

where r is one from the 6 possible neighbour voxels, and variables $\mathbf{N}^r_{n_{\text{mig}},t}$ and $\mathbf{P}_{\text{dist},r}$ (in bold font) represent vectors of r components (as many as neighbours).

Tumour volume was computed as the number of voxels that contained more than a threshold number of cells. Tumour activity was computed as the number of newborn cells at each time step.

For the simulations analyzed in this study, a cubic grid of 80 elements per side was selected, so there were 5.12×10^5 voxels available for cells to invade them. We considered four different clonal populations, each of them being more aggressive than the previous one. Cells from population 1 could mutate into populations 2 or 3, but population 4 was only accessible through these two. Initially, a single cell belonging to clonal population 1 was placed in the central voxel of the computational domain. Each voxel measured 1 mm^3, in line with typical voxel sizes available in high spatial resolution morphological imaging. Thus, our computational volume was 512 cm^3, enough to explore tumour sizes from undetectable to life-incompatible in some tumour types. Simulations were stopped once the tumour volume reached values of $V_{end} = 100$ cm^3.

The whole set of parameters considered in our simulations is displayed in Table S1. Additionally, the weights that modulate the different processes rates for each clonal population are shown in Table S2 as ratios compared to clonal population 1. In this paper we wanted to focus on the metabolic dynamics and the emergence of superlinear scaling laws, however the mesoscale simulator has been proven to be useful to describe the particular dynamics of specific tumour types. For instance, for glioblastomas, once the subpopulations were related to the most frequent molecular alterations/subgroups and the parameters fitted accordingly the mesoscale simulator provided a picture of the growth of these tumours resembling closely their growth dynamics. Results will be reported elsewhere.

The simulator was implemented in Julia (version 1.1.1). Simulations were performed on a network of 12-core 64 GB memory 2.7 GHz Mac Pro and a 12-core 128 GB memory 2.0 GHz iMac Pro machines. Computational cost per simulation was of about 2 hours per run in single-processor mode.

S4. Study of Partial-Volume Effects.

The term "partial-volume effect (PVE) refers to several effects that make intensity values in PET images differ from their correct values [5]. The first effect is the image blurring introduced by the spatial resolution of the imaging system. This causes spillover between regions, and leads to larger but dimmer images for small regions. Part of the signal from the source "spills out and hence is seen outside the actual source. A second source of image blurring is image sampling. The voxel contours do not match the actual contours of the tracer distribution. Thus, the signal intensity in each voxel is the mean of the intensities of the different tissues included in that voxel. In our case, and since the PVE is larger for smaller sources there could be an apparent increase in the MTVs that would be relatively larger for smaller volumes. This could result in an apparent increase of the slope of the scaling law that is difficult to quantify a priori. This is why we restricted our analysis to tumours with diameters larger than 2 cm corresponding to volumes larger than 4 cm^3. However, to exclude the PVE as potentially being the cause of the observed superlinear behaviour, we performed several computational studies.

First, we calculated the scaling exponents for two additional sets of tumours: those with diameters larger than 2.5 cm and 3.0 cm respectively. The results obtained are summarized for breast cancer in Table S3 for patients imaged with ^{18}F-FDG and Table S7 for patients imaged with ^{18}F-FLT. We also provide the results for lung cancer (Table S4), head and neck cancer (Table S5) and rectal cancer (Table S6). We excluded from the analysis gliomas since they typically contain large necrotic areas and the active tumour regions are often rim-like, thus PVE effects, if present, will not be related to the tumour diameters. For the other tumour histologies studied, having more compact shapes, there were either no or very few tumours with necrotic areas.

We did not find a reduction in the β values as the cutoff tumour size was increased, that could evidence an impact of the PVE. Instead, fluctuations in the obtained values around the original superlinear values and a trend towards a reduction of the R^2 value and an increase in the standard deviation as the number of patients was decreased were observed.

Next, we performed an additional test to assess possible PVE. Since the blurred areas around the main tumour core could be partially affected by PVE, we carried out segmentations of the core tumour areas (either manually or using the automatic segmentation algorithm with $\lambda = 0$) for a subset of the tumour histologies and compared the results with those obtained with either the automatic segmentation with ($\lambda \neq 0$) or a manual one including the lower SUV part halo around the tumour.

We performed this last study for three tumour histologies. Results for lung cancer patients imaged with ^{18}F-FDG are summarized in Table S8. There the comparison was carried out between the standard automatic procedure and the automatic procedure without the inclusion of the surrounding lower SUV values halo around the tumour core ($\lambda = 0$, see 'Methods'). The exponents obtained were superlinear with overlapping intervals. In the second series of tests, for breast cancer patients imaged with ^{18}F-FDG, we compared the results of the standard automatic segmentation with the one choosing $\lambda = 0$ and a manual segmentation performed choosing only the higher value SUV areas. Results are shown in Table S9. The three values obtained were in line with the exponent reported in the main text, and in any case showed superlinear behaviour. A final comparison was performed for the colon cancer patients for which no automatic segmentation could be performed due to the proximity of confounding structures. There, two manual segmentations were done, one of them including the whole tumour and a second one restricted to the core higher SUV value areas. Results are summarized in Table S10. The values were compatible within them and with the superlinear dynamics.

In summary, although the PVE is always present in PET images and could potentially affect the obtained scaling exponents, it appears that for our scanners and type of study the choice of a minimal tumour size of 2 cm was enough to guarantee a minor impact of this effect.

S5. Automatic Segmentation algorithm for PET images

An automatic segmentation algorithm was designed and implemented in Matlab to carry out the segmentations of tumours in patient subgroups 1, 4, and 6.

Each PET image contains a spatial map of the SUV activity ($u(\vec{x})$). Each SUV threshold defines an isosurface in the function u. This means that the isosurfaces are parametrized by the threshold values (u_*) and all of the threshold-based potential segmentations of the bulk tumour are indeed isosurfaces of $u(\vec{x})$. The contour that better delineates the tumour is the one that maximizes the contrast in the image over the adjacent isosurfaces. To quantify this, we used the functional

$$\mathcal{F}(u_*;\lambda) = (1-\lambda u_*)\int_{\{\vec{x}/u(\vec{x})=u_*\}} |\nabla u|^2\, dS, \qquad \text{(S34)}$$

that was computed for each image and each possible threshold value u_*. The surface integral of the squared gradient quantifies the variation in SUV over the isosurface of SUV level u_*. The factor $(1-\lambda u_*)$ was chosen to penalize higher SUV values in order to get a more accurate delineated zone. For each image, the functional (S34) was computed for every possible threshold value u_* from the maximum SUV in the image. The value u_* that maximizes (S34) was then selected as segmentation threshold and, therefore, the corresponding isosurface used as bulk segmentation. This is an example of variational, gradient based segmentations that have been used in the literature of PET segmentation such as the method of snakes [6,7], although in three-dimensional scenarios and restricting the contours to isosurfaces.

The value of the parameter $\lambda = 0.26$ was selected by performing an optimization process where a set of breast and lung tumour segmentations performed by a board of three imaging engineers were used as ground truths and compared to those provided by variable values of λ. Note that the case $\lambda = 0$ corresponds to the choice of the tumor areas with stronger gradients and allows for the segmentation of the tumor core, excluding the lower densities halos surrounding the higher SUV values tumor regions.

Dataset	Fitting exponent (β)	Std deviation	Number of patients	R^2
> 2.0 cm	1.307	0.069	54	0.87
> 2.5 cm	1.331	0.084	51	0.83
> 3.0 cm	1.211	0.124	37	0.73

Table S3 Comparison of the scaling exponent β obtained for breast cancer patients imaged with ^{18}F-FDG and different lesion size cutoff values

Dataset	Fitting exponent (β)	Std deviation	Number of patients	R^2
> 2.0 cm	1.248	0.032	175	0.90
> 2.5 cm	1.206	0.045	133	0.84
> 3.0 cm	1.261	0.064	92	0.81

Table S4 Comparison of the scaling exponent β obtained for lung cancer patients imaged with ^{18}F-FDG and different lesion size cutoff values

Dataset	Fitting exponent (β)	Std deviation	Number of patients	R^2
> 2.0 cm	1.182	0.030	76	0.87
> 2.5 cm	1.229	0.067	50	0.87
> 3.0 cm	1.300	0.097	40	0.82

Table S5 Comparison of the scaling exponent β obtained for head and neck cancer patients imaged with ^{18}F-FDG and different lesion size cutoff values

Dataset	Fitting exponent (β)	Std deviation	Number of patients	R^2
> 2.0 cm	1.386	0.152	23	0.80
> 2.5 cm	1.471	0.159	22	0.81
> 3.0 cm	1.712	0.224	20	0.76

Table S6 Comparison of the scaling exponent β obtained for rectal cancer patients imaged with ^{18}F-FDG and different lesion size cutoff values

Dataset	Fitting exponent (β)	Std deviation	Number of patients	R^2
> 2.0 cm	1.188	0.035	75	0.92
> 2.5 cm	1.147	0.046	60	0.91
> 3.0 cm	1.096	0.065	44	0.87

Table S7 Comparison of the scaling exponent β obtained for breast cancer patients imaged with ^{18}F-FLT and different lesion size cutoff values

Segmentation procedure	Fitting exponent (β)	Std deviation	Number of patients	R^2
Standard automatic	1.248	0.032	175	0.90
Only core ($\lambda = 0$) automatic	1.192	0.047	169	0.79

Table S8 Comparison of the scaling exponent β obtained for lung cancer patients imaged with ^{18}F-FDG with different segmentation procedures. The automatic algorithm failed to provide consistent results with $\lambda = 0$ for six patients and were excluded from the analysis.

Segmentation procedure	Fitting exponent (β)	Std deviation	Number of patients	R^2
Standard automatic	1.307	0.069	54	0.87
Only core ($\lambda = 0$) automatic	1.233	0.094	54	0.76
Only core (manual)	1.255	0.052	54	0.91

Table S9 Comparison of the scaling exponent β obtained for breast cancer patients imaged with ^{18}F-FDG with different segmentation procedures.

Segmentation procedure	Fitting exponent (β)	Std deviation	Number of patients	R^2
Manual (whole tumour)	1.386	0.152	23	0.80
Manual (only core)	1.307	0.137	23	0.82

Table S10 Comparison of the scaling exponent β obtained for rectal cancer patients imaged with ^{18}F-FDG with different segmentation procedures.

For the application of the method, a point belonging to the tumour has to be chosen initially. While the isosurface of a given value might be extensive along the domain, only the part enclosing the initial point are taken into account for the calculations. After having selected the points the SUV range for the image is divided in 512 equally distributed partitions which constitute a discretization for the possible threshold points u_*. The functional (S34) is then applied using descending values for u_* starting from SUVmax. The process is continued until a local maximum for $\mathcal{F}(u_*;\lambda)$ is found. When this maximum is followed by a concatenation of five points with a strictly descending tendency the algorithm stops and the u_* that maximizes the functional is used as threshold value.

References

[1] West, G.B., Brown, J.H., Enquist, B.J. A general model for ontogenetic growth. *Nature* **413**, 628-631 (2001).

[2] Murray, J.D. *Mathematical Biology.* Third Edition. (Springer-Verlag, Berlin, 2002).

[3] Hanahan D., & Weinberg, R. A. Hallmarks of cancer: the next generation. *Cell* **144,** 646-674 (2011).

[4] Pérez-Beteta, J. et al. Tumor surface regularity at MR imaging predicts survival and response to surgery in patients with glioblastoma. *Radiology* **288,** 218-225 (2018).

[5] Soret, M., Bachrach, S.L., Buvat, I. Partial-Volume Effect in PET Tumor Imaging. *J Nucl Med* **48**, 932-945 (2007).

[6] Kass, M., Witkin, A. & Terzopoulos, D. Snakes: active contour models. *Int. J. Comput. Vis.* **1,** 321-331 (1987).

[7] Zaidi, H. & El Naqa, I. PET-guided delineation of radiation therapy treatment volumes: a survey of image segmentation techniques. *Eur. J. Nucl. Med. Mol. Imaging* **37,** 2165-2187 (2010).